

Analysis of the crack formation in ASIS M2 high-speed tool steel during utilization

Kozina, Franjo; Zovko Brodarac, Zdenka; Jandrlić, Ivan; Jagustović, Renato

Source / Izvornik: **Proceedings book of 19th International Foundrymen Conference, 2021**

Conference paper / Rad u zborniku

Publication status / Verzija rada: **Published version / Objavljena verzija rada (izdavačev PDF)**

Permanent link / Trajna poveznica: <https://urn.nsk.hr/urn:nbn:hr:115:601528>

Rights / Prava: [In copyright](#) / [Zaštićeno autorskim pravom.](#)

Download date / Datum preuzimanja: **2025-03-23**



SVEUČILIŠTE U ZAGREBU
METALURŠKI FAKULTET
UNIVERSITY OF ZAGREB
FACULTY OF METALLURGY

Repository / Repozitorij:

[Repository of Faculty of Metallurgy University of Zagreb - Repository of Faculty of Metallurgy University of Zagreb](#)





ANALYSIS OF THE CRACK FORMATION IN ASIS M2 HIGH-SPEED TOOL STEEL DURING UTILIZATION

Franjo Kozina^{1*}, Zdenka Zovko Brodarac¹, Ivan Jandrić¹, Renato Jagustović²

¹ University of Zagreb Faculty of Metallurgy, Sisak, Croatia

² DIV GRUPA d.o.o., Samobor, Croatia

Abstract

Tool steels are carbon, alloyed or high-speed steels, produced and processed under the tool steel manufacturing practices to meet special requirements. The advancements in tool steel engineering properties enabled work efficiency improvements in industrial applications. The high-speed tool steels (HSS) are complex iron-based alloys containing carbon, chromium, vanadium, molybdenum, tungsten or substitutional amount of cobalt. The chemical composition of HSS is designed to achieve the highest attainable hardening response, high wear resistance, high resistance to softening effect at elevated temperatures, and good toughness necessary for effective use in industrial cutting operations. The ASIS M2 is a molybdenum-based medium alloyed HSS with good machinability. Favorably designed chemical composition and adequately performed heat treatment assure good combination of toughness, wear resistance and hardness enabling its utilization as twist drills, taps, milling cutters, saws, and knives. It is also commonly used as cold work punches. The research was performed on two samples of ASIS M2 punches to estimate the cause of the shorter service life. In sample 1 the crack nucleation occurred after 50.000 punched marks, while in sample 2 cracking initiated after 20.000 punched marks. To indicate the cause of sample 2 shorter service life, the results of chemical composition analysis, metallographic analysis, and microhardness measurements were compared. The higher amount of carbide forming elements in sample 2 led to the solidification of higher number of eutectic carbides and precipitation of secondary carbides in intercellular regions. The microstructure analysis indicated significantly higher number of carbide particles in sample 2. The presence of carbide particles led to the texture development and impacted crack propagation direction. Higher amount of carbide particles in sample 2 caused higher crack dissipation and material layering with a decrease in crack propagation depth and shorter service life.

Keywords: ASIS M2, high-speed tool steels, cracking, service life, microstructure, carbides

*Corresponding author: fkozin@simet.unizg.hr

INTRODUCTION

The industrial utilization of tool steels with improved engineering properties, such as high-speed tool steels (HSS), enabled work efficiency improvement [1]. Tool steels are carbon,

alloyed or high-speed steels, produced and processed under the tool steel manufacturing practices to meet special requirements. This type of steels is used in hand tools or in mechanical fixtures to cut, shape, form, or blank materials at room or elevated temperatures. Based on their final application tool steels can be classified as hot work tool steels, cold work tool steels, plastic mold steels, and HSS [2]. Due to their ability to machine materials at high cutting speeds [3], HSS are commonly used to manufacture broaches, drills, millings, cutters, tool bits, gear cutters, saw blades, jointers and planar blades [4]. The HSS are complex iron-based (Fe) alloys containing carbon (C), chromium (Cr), vanadium (V), molybdenum (Mo), tungsten (W) and in some steel types a substitutional amount of cobalt (Co). The chemical composition is designed to achieve highest attainable hardening response, high wear resistance, high resistance to softening effect at elevated temperatures, and good toughness necessary for effective use in industrial cutting operations [5]. The American Iron and Steel Institute (AISI) established an HSS classification system based on chemical composition [6]. That system consists of a letter and numerical designation. The letter designation can be either T or M. The T designation is provided for HSS containing W as one of the primary alloying elements (12 wt.% to 20 wt.% W), while M refers to steels containing higher amounts of Mo (3.4 wt.% to 10 wt.% Mo). The numerical designation is used to distinguish between the classes based on the presence of other major alloying elements [7]. The C, Cr, V and Co are considered to be other major alloying elements in HSS [8]. The M class of HSS has higher absorption resistance, better dimensional stability during heat treatment and are less expensive compared to T class [6]. The most important and closely controlled alloying element is C. Although, C content in any type of HSS is fixed within the narrow limits, variations within those limits can cause important changes in the mechanical properties and steel's cutting ability. Increase in C content increases working hardness, elevated temperature hardness, and wear resistance. This increase in mechanical properties, especially hardness, is a consequence of eutectic carbide solidification and precipitation of secondary carbides during heat treatment [6]. The MC, M_2C , M_6C and M_7C_3 (M refers to the strong carbide forming elements) are coarse and blocky carbides that solidify during eutectic reaction [9]. The solidification of austenite (γ_{Fe}) and eutectic carbides is a consequence of reduced solid solubility of C in ferrite (α_{Fe}) solid solution. While MC type of eutectic carbides mostly solidifies inside the solidification cells, the M_2C , M_6C and M_7C_3 form network in the intercellular regions [10]. The secondary carbides precipitate because of the eutectic carbide decomposition during heat treatment. Decomposition of eutectic M_2C carbide comprehends peritectoid and eutectoid precipitation of MC and M_6C secondary carbides [11]. While the primary function of eutectic carbides is to increase the wear resistance, secondary carbides improve strength at elevated temperatures. However, the thermal fatigue and fracture toughness cannot be influenced by eutectic to secondary carbide decomposition because MC and M_6C carbides retain M_2C eutectic carbide morphology. The W, Mo and V are strong carbide forming elements [12]. In all T types of HSS W is the major alloying element, and it is present in all M types of HSS as auxiliary element, except in M10 with regular or high C content. By forming hard complex W_2C , Fe_3W_3C and Fe_4W_2C carbides [13], W contributes to wear resistance, elevated temperature hardness and causes secondary hardening [14]. The M types of steels with higher Mo content have lower melting points and require lower hardening temperatures. Consequently, they have more narrow hardening range compared to T types of HSS. Like W, the Mo forms simple Mo_2C [15] and complex Mo_3Fe_3C and Mo_4Fe_2C carbides [16]. Since the Mo ($Ar(Mo) = 95.939 \text{ g/mol}$ [17]) has half atomic weight of W ($Ar(W) = 183.85 \text{ g/mol}$ [18]), the preferred formation of Mo-based carbides is expected. Therefore, the M types of HSS have higher toughness and lower elevated

temperature hardness. The improvement in elevated temperature stability can be addressed through the additions of W or V [6]. The V additions promote the formation of very hard, stable VC carbides [19] that increase wear resistance and elevated temperature hardness [6]. The object of heat treatment is to transform a fully annealed HSS microstructure consisting of α_{Fe} and eutectic M_xC_y carbides into a hardened and tempered martensitic microstructure (α_{Fe}') containing secondary carbides that provide required properties. The HSS heat treatment can be divided into preheating, austenitizing, quenching and tempering. The preheating reduces thermal shock, carburization/decarburization and increases productivity with no direct influence on hardening reactions. The austenitizing is the second step in HSS heat treatment enabling dissolution of eutectic carbides and property development [20]. The eutectic carbide dissolution occurs at the temperatures between 1150°C and 1290°C with a holding time of 2 min to 6 min, depending upon HSS type, tool configuration and cross-section size [6]. The quenching or rapid cooling is designed to transform γ_{Fe} into a hard α_{Fe}' microstructure. The cooling rate is dictated by the type of steel and is strictly controlled. After quenching steel is in a highly stressed condition and susceptible to cracking [21]. To relieve stress, increase toughness and provide secondary hardening the HSS is tempered. The tempering involves reheating the steel to an intermediate temperature (below the critical transformation temperature), soaking and air cooling. The secondary hardening is obtained by the transformation of retained γ_{Fe} into α_{Fe}' and precipitation of complex secondary carbides. This subsequent transformation and precipitation require multiple tempering procedures specific to a particular HSS type [22]. The heat treatment of ASIS M2 with regular C comprehends preheating at the temperatures between 732°C and 843°C followed by austenitization at 1227°C. The austenitization of ASIS M2 with high C is performed at lower temperature (1216°C). The ASIS M2 can be tempered at 538°C or 552°C. If the ASIS M2 is tempered at 538°C the tempering needs to be repeated four times with a soaking time of 2 h. Tempering at 552°C is repeated two times with a soaking time of 2h [7].

The goal of this paper is to analyze the cause of the crack formation in ASIS M2 high speed tool steel punchers during utilization. The research was performed on two samples (sample 1 and sample 2). The crack formation in sample 1 was observed after 50.000 punched marks. Contrary, in sample 2 the cracks initiated after only 20.000 punched marks. By comparing the results of chemical composition analysis, metallographic analysis, and microhardness measurements the cause of the sample 2 shorter service life was indicated.

MATERIALS AND METHODS

The chemical composition of the ASIS M2 samples was determined spectroscopically using Optical emission spectrometer Analytical Instruments Group (GNR) S7 metal Lab Plus (MLP). The chemical composition of ASIS M2 HSS according to ASTM A 600 – 92a is given in Table 1.

Table 1. The Chemical composition of HSS M2 according to ASTM A 600 – 92a, wt.% [7]

HSS		C	Mn	P	S	Si	Cr	V	W	Mo	Co
M2 regular C	min	0.78	0.15	/	/	0.20	3.75	1.75	5.50	4.50	/
	max	0.88	0.40	0.03	0.03	0.45	4.50	2.20	6.75	5.50	/
M2 high C	min	0.95	0.15	/	/	0.20	3.75	1.75	5.50	4.50	/
	max	1.05	0.40	0.03	0.03	0.45	4.50	2.20	6.75	5.50	/

Based on the chemical composition ASIS M2 is divided into two subcategories: ASIS M2 with regular C (0.78 wt.% - 0.88 wt.% C) and ASIS M2 with high C (0.95 wt.% - 1.05 wt.% C) (Table 1). The difference in the content of other alloying elements cannot be observed (Table 1).

The metallographic analysis was performed to determine macrostructure and microstructure of the samples in polished and etched conditions. The metallographic analysis in polished condition was performed to assess the crack nucleation and progression as well as the occurrence of additional defects in the samples of HSS. The macrostructure analysis in the etched condition was used to indicate the influence of tool production and heat treatment on the structure development, while the microstructure analysis enabled phase identification and homogeneity assessment of the affected area.

The sampling for metallographic analysis is given in Figure 1.



Figure 1. Sampling for metallographic analysis: a) sample 1, b) sample 2

In both samples' cracks can be observed on the tools' surface at the sharp transition between the outer edge and the contact surface (Figure 1). When marking the screw, the outer edge of the tool serves to position and hold the screw while the contact surface marks the screw's head. Cracks in sample 1 occurred after 50.000 punched marks while in sample 2 they occurred after 20.000 punched marks.

The sampling was performed perpendicular to the cracks' propagation direction (Figure 1). The samples were etched after standard metallographic preparation comprehending grinding and polishing. Two different solutions were used for etching:

1. The 2 % Nital (the 2 % solution of nitric acid (HNO_3) in ethyl alcohol ($\text{C}_2\text{H}_5\text{OH}$))
2. The Marshall's reagent consisting of two different solutions:
 - a. Solution containing 5 ml of sulfuric acid (H_2SO_4), 8 g of oxalic acid ($\text{C}_2\text{H}_2\text{O}_4$) and 100 ml of water (H_2O)
 - b. 30 % aqueous solution of hydrogen peroxide (H_2O_2).

The 2 % Nital was used as a general-purpose etchant for macrostructure and microstructure analysis. The Marshall's reagent is obtained by mixing equal parts of solution a and b

immediately before etching. The Marshall's reagent was used for qualitative and quantitative phase analysis. The qualitative analysis comprehended the phase identification based on coloring. The quantitative analysis involved determining the amount of the identified phases and the phase classification with concerning the particle size. The identified phases were distributed into 5 classes: Class 1 (0.5-4.40 μm^2), Class 2 (4.40-8.30 μm^2), Class 3 (8.30-12.20 μm^2), Class 4 (12.20-16.10 μm^2), Class 5 (16.10-20.0 μm^2). Besides phase analysis, the Marshall's etching solution enabled observation of the apparent austenitic grain boundaries in the martensitic matrix. The austenitic grain size was measured using the Linear intercept method according to ASTM E 112-10. The Linear intercept method implies drawing the reference line with the length (L) and counting the cross-section of the line and the grain boundaries (P_L). The line is drawn so that a single grain is intersected only once. After calculating the number of intersections per mm of the reference line (P_L), the apparent size of the austenitic grain (G) is determined based on the equation 1:

$$G = - 3.2877 + 6.6439 \log_{10} P_L \quad (1)$$

Where G is the ASTM grain size number and $- 3.2877$ and 6.6439 are constants relating P_L and magnification to G.

The macrostructure analysis of the samples was performed on the Olympus SZ11 stereo microscope equipped with a Promicra digital camera and the QuickPHOTO CAMERA 3.1 image processing software. Microstructure analysis was performed on the Olympus BX51 inverted metallographic microscope equipped with a DP70 digital camera and the AnalySIS Materials ResearchLab software.

The microhardness measurements were performed after metallographic analysis. The microhardness was measured in the area of the defect and in non-affected area of the samples 1 and 2. The Vickers method with a load of 9.81 N on a Leica VMHT device was used to measure the microhardness.

RESULTS AND DISCUSSION

Results of chemical composition analysis

The results of chemical composition analysis are given in Table 2.

Table 2. The chemical composition of the samples 1 and 2

Sample	C	Mn	P	S	Si	Cr	V	W	Mo	Co	Fe
1	0.864	0.305	0.022	<0.001	0.235	4.076	1.697	6.295	4.890	0.640	Balance
2	0.855	0.349	0.029	0.002	0.434	4.374	1.841	6.618	5.245	0.727	Balance

The chemical composition of both samples (Table 2) is in accordance with ASTM A 600 – 92a Standard Specification for Tool Steel High Speed (Table 1). Based on the slightly higher C content, better hardenability of sample 1 is expected (Table 2). The higher amount of carbide forming elements suggests higher share of carbides in sample 2 (Table 2).

Results of macrostructure analysis

The macrostructure of the sample 1 in polished and etched condition is given in Figure 2 a and b. The details for subsequent microstructure analysis in polished end etched conditions are indicated in Figure 2 a.

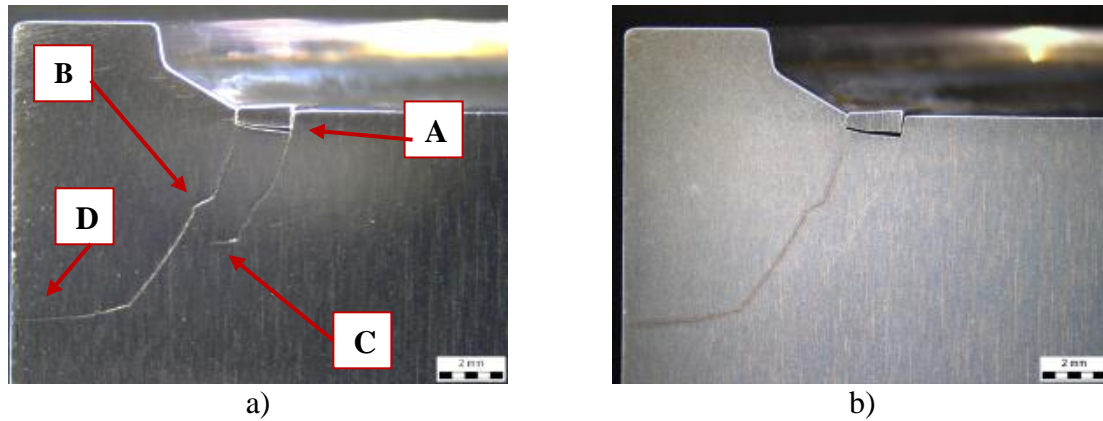


Figure 2. Macrostructure of the sample 1 in: a) polished condition with indicated details (A, b, C, and D) for subsequent microstructure analysis, b) etched condition

Two cracks are present in the macrostructure of the sample 1. Cracks initiate on the surface at the sharp transition between the outer edge and the contact surface of the tool (Figure 2). The cracks propagate perpendicular to the contact surface to a depth of 6.43 mm (Figure 2, crack left) and 4.14 mm (Figure 2, crack right). After that, the cracks change direction and progress parallel to the contact surface. The crack to the left propagates outside of the tool (Figure 2 a). In the area between the cracks, the surface layer is separated (Figure 2). After etching the texture can be observed in the macrostructure of the sample 1. The texture is perpendicular to the surface of the tool (Figure 2 b). Although the structure is not homogeneous, no significant difference between the surface and central part of the tool can be observed (Figure 2 b).

The *Multiple Image Alignment* (MIA) of the sample 1 in polished and etched condition is given in Figure 3.

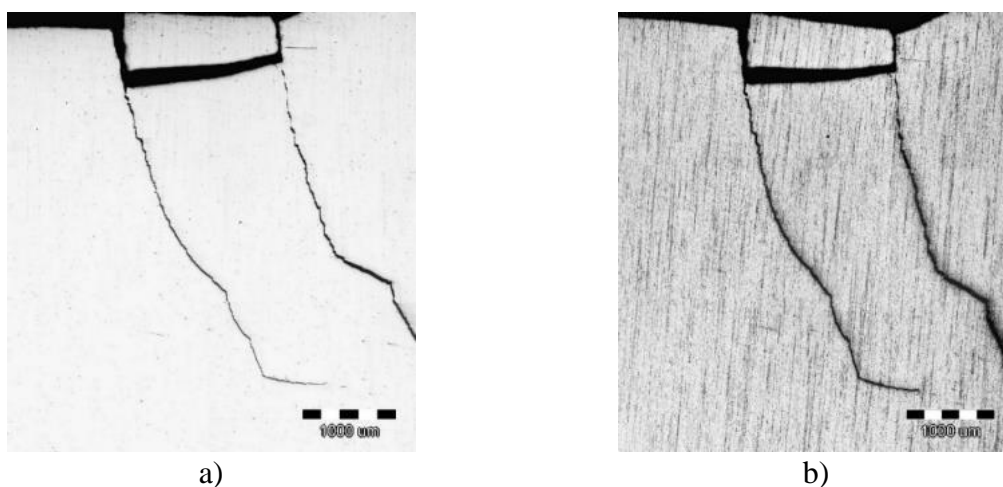


Figure 3. The MIA of the sample 1 in: a) polished, b) etched condition

Apart from the cracks and the separation of the surface layer between the cracks, there are no other visible defects present in the macrostructure of the polished sample (Figure 3 a). After etching, the texture can be observed in the microstructure of the sample 1 affecting the crack propagation direction. The texture affects the crack propagation direction. No other heterogeneities of macrostructure can be detected in the macrostructure of the area of the defect (Figure 3 b).

The macrostructure of the sample 2 in polished and etched condition with indicated details for subsequent microstructure analysis are given in Figure 4.

Three cracks can be seen in the macrostructure of sample 2. Cracks nucleate at the marking grooves of the contact surface. The cracks progress perpendicular to the tool's contact surface to a depth of 3.21 mm (crack left) and 3.24 mm (crack right), respectively. After that, the cracks change direction and progress parallel to the contact surface (Figure 4 a). The cracks on the left at a depth of 1.75 mm merge into one crack and propagate towards the center of the tool (Figure 4 a). At the depth of 3.67 mm crack on the right and crack on the left merge and propagate parallel to the contact surface of the tool (Figure 4 a). After etching the texture can be observed in the macrostructure of the sample 2. The texture is perpendicular to the surface of the tool (Figure 4 b).

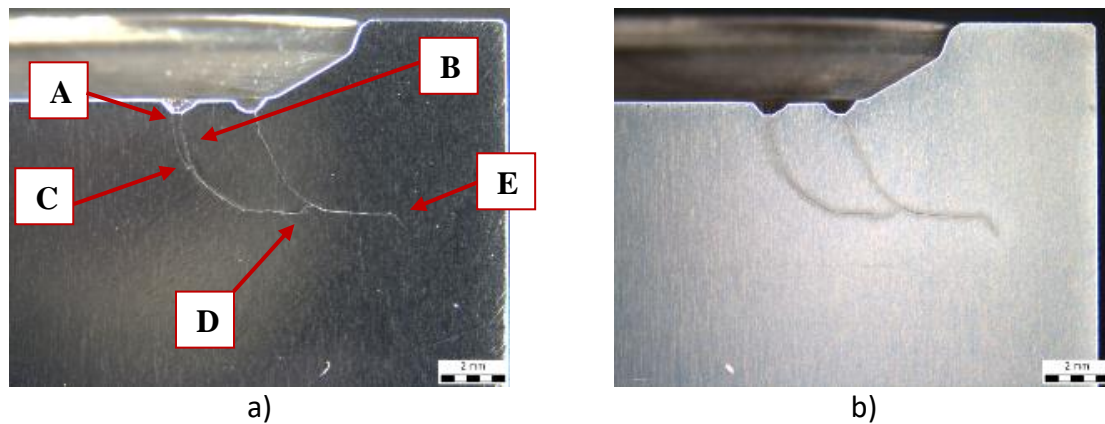
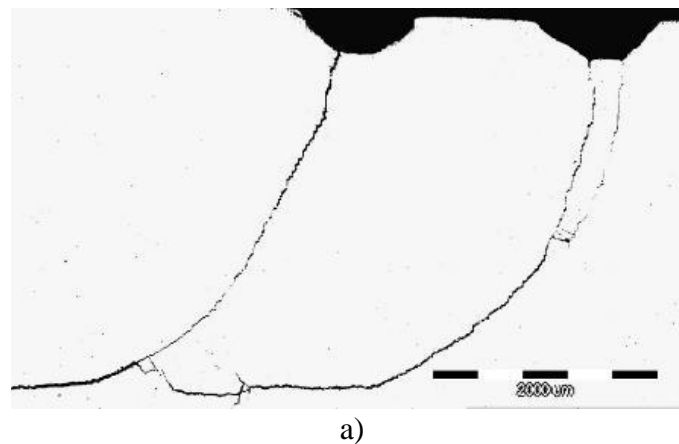


Figure 4. Macrostructure of the sample 2 in: a) polished condition with indicated details for subsequent microstructure analysis, b) etched condition

The MIA of sample 2 in polished and etched condition is given in Figure 5.



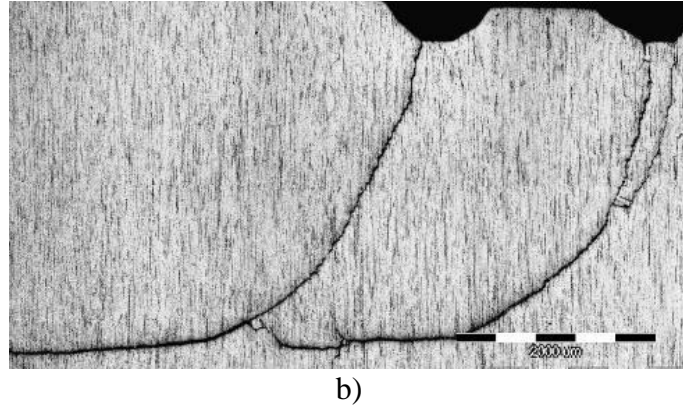
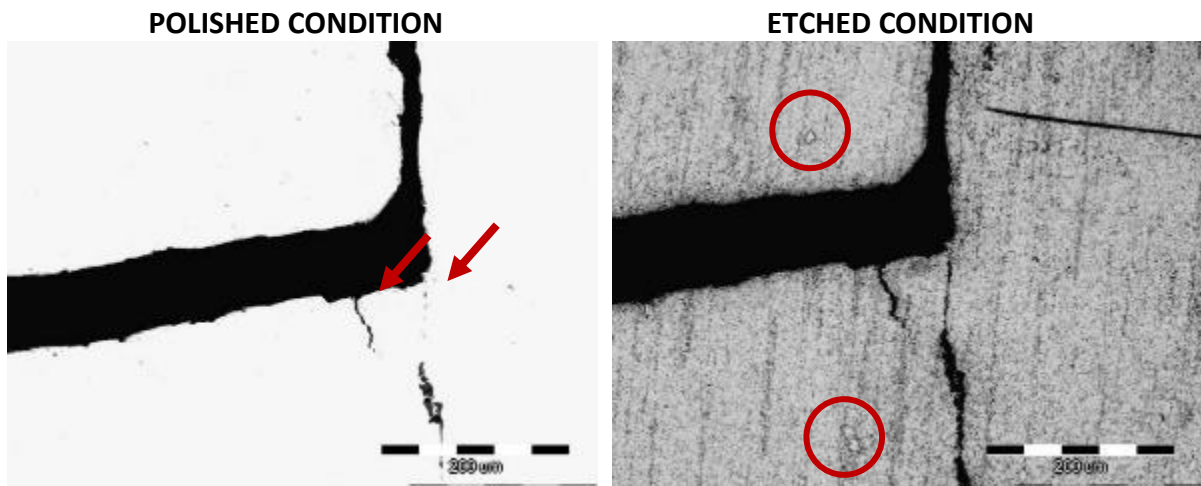


Figure 5. The MIA of the sample 2 in: a) polished, b) etched condition

In contrary to the sample 1, the cracks in sample 2 show a greater tendency towards branching and material layering (Figure 5 a). Due to the energy dissipation, the crack propagation in the sample 2 is not as deep as in sample 1. Apart from the crack, there are no other visible defects in the macrostructure of sample 2. Etching of the sample revealed a texture affecting the crack propagation direction. No other heterogeneities are observed in the macrostructure of the sample 2 (Figure 5 b).

Results of microstructure analysis

The microstructure of the sample 1 in polished and etched conditions is shown in Figure 6. The details for microstructure analysis were indicated in Figure 2 a.



Detail A

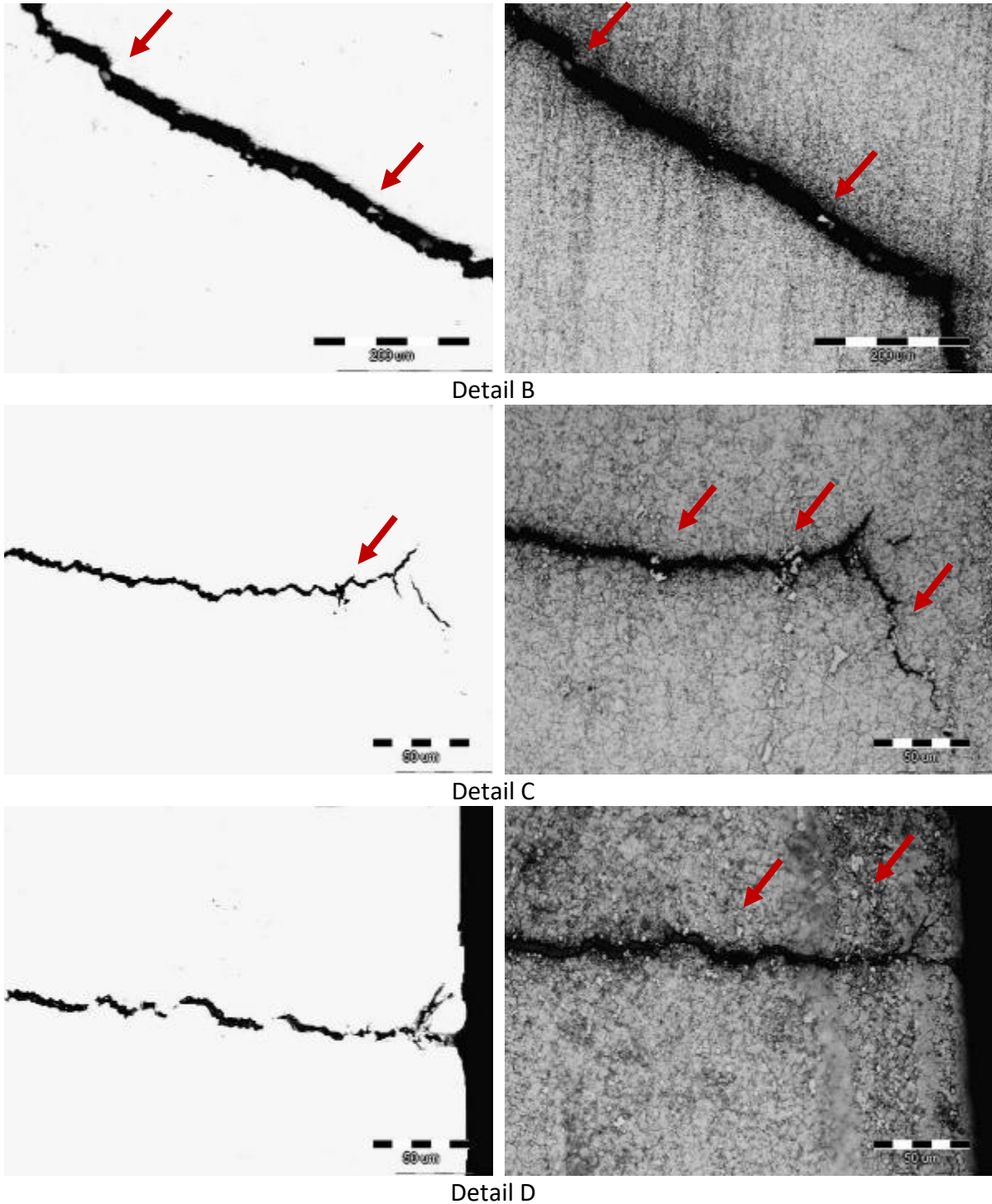
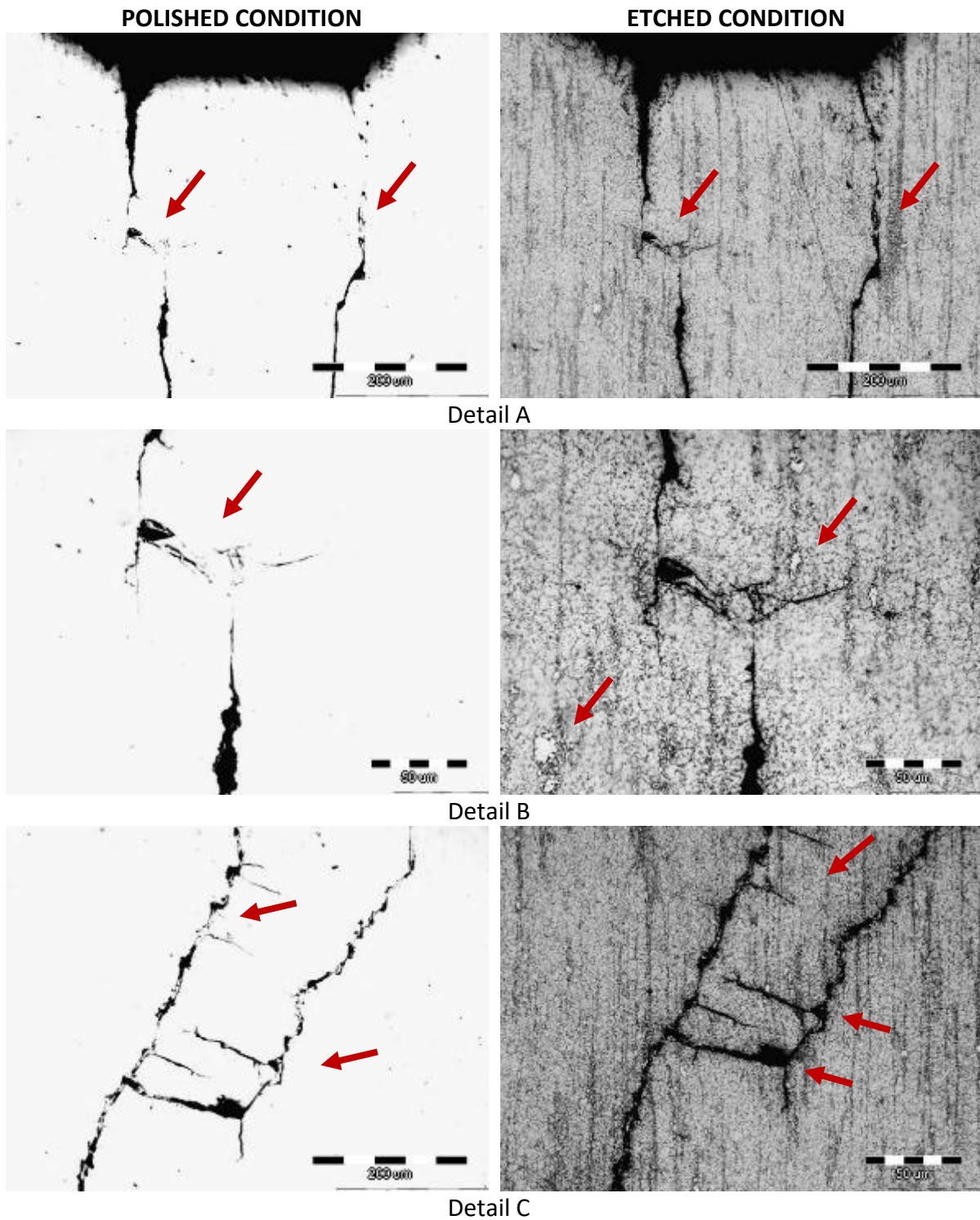


Figure 6. Microstructure of sample 1 in the area of the defect

The branching of the cracks occurs in the area of the surface layer separation. The crack branches propagate perpendicular to the work surface of the sample (Figure 6 detail A, polished condition). The matrix is martensitic with the particles located in the intercellular regions (Figure 6, etched condition). Besides particles with fine morphology, coarse particles are also present in the microstructure of sample 1. The nucleation and growth of these particles is associated with texture formation (Figure 6, etched condition). These particles can be observed near (Figure 6 detail A, etched condition) and inside the cracks (Figure 6 details

B, C, D, polished and etched condition) influencing their propagation direction. The presence of the particles inside the cracks indicates intercrystal crack propagation (Figure 6).

The microstructure of the sample 2 in polished and etched condition is shown in Figure 7. The details for microstructure analysis are indicated in Figure 4 a.



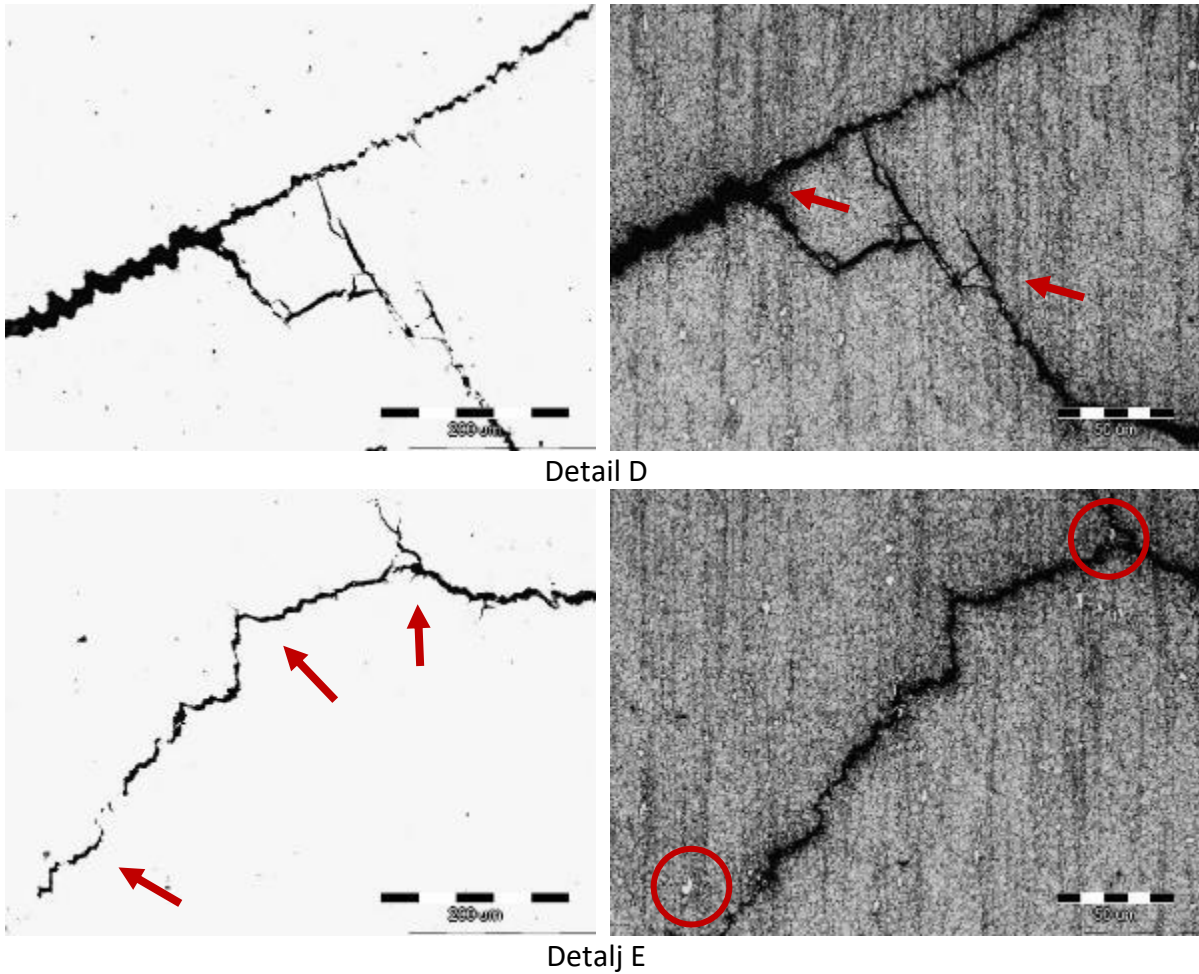
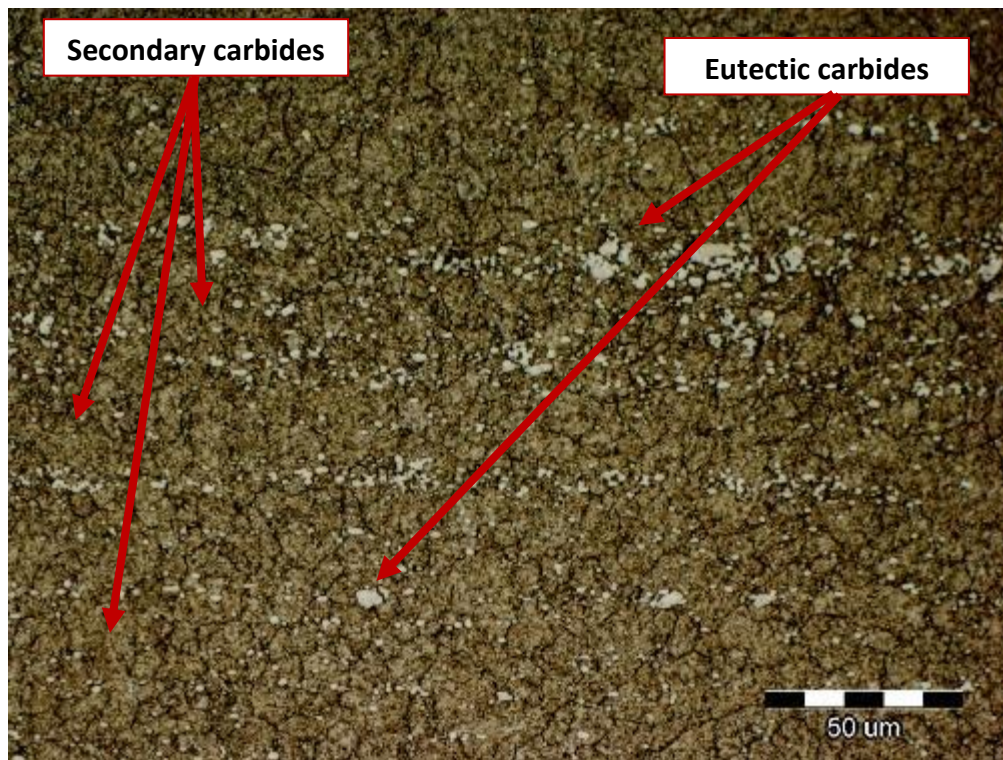


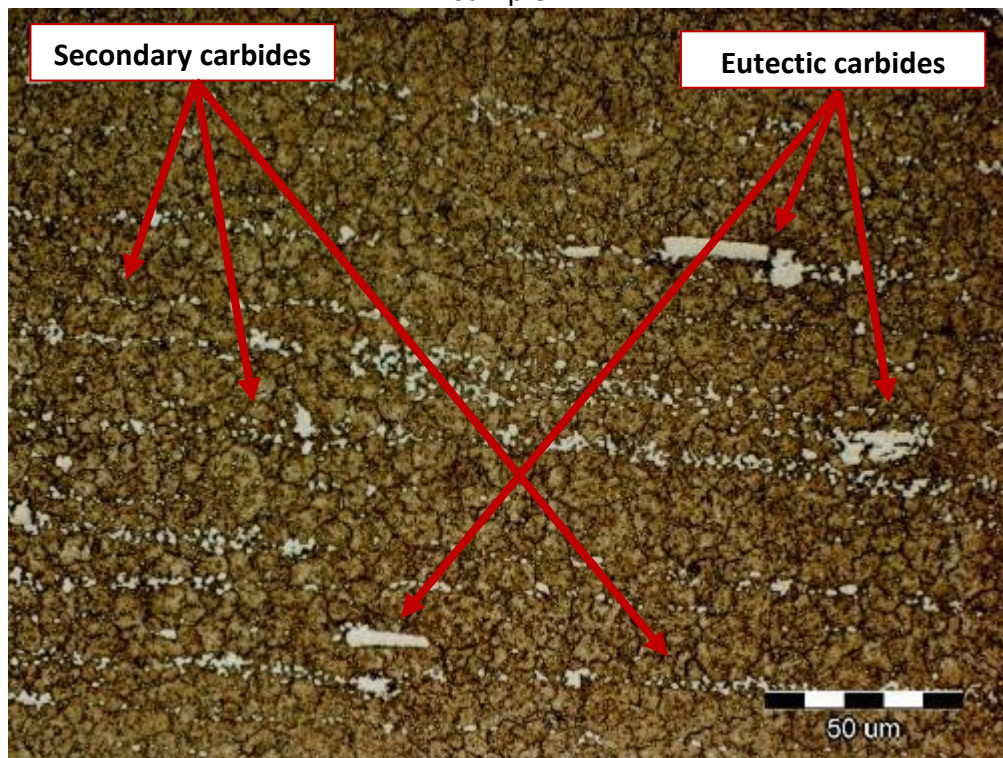
Figure 7. Microstructure of sample 2 in the details indicated in Figure 4 a

In sample 2, the crack nucleates at the work surface of the tool and progresses parallel to the texture direction. The material layering and cavity formation can be observed near the surface of the sample (Figure 7, polished condition). In this area, the existing crack dissipates followed by the nucleation of new cracks. The matrix of sample 2 is martensitic with fine particles located in the intercellular regions (Figure 7, etched condition). The nucleation and growth of coarse particles is connected to the texture development. In contrast to sample 1, cracks in sample 2 show a greater tendency towards branch and material layering (Figure 7 detail C, D, E, polished state). Initial cracks and branches of initial cracks propagate through the grain boundaries (Fig. 8 detail C, D, E, corroded state).

The microstructure of the sample 1 and 2 after etching with Marshall's etching solution is given in Figure 8.



Sample 1



Sample 2

Figure 8. The microstructure of sample 1 and 2 after etching with Marshall's etching solution.

The use of Marshall's etching solution enabled identification of coarse particles as eutectic carbides. The fine particles precipitated at the apparent austenite grain boundaries are secondary carbides. Both primary and secondary carbides have preferred orientations (Figure 8). The matrix of both samples is martensitic with indicated apparent austenite grain

boundaries (Figure 8.). The results of quantitative carbide particle analysis, performed on five different micrographs, are shown in Table 3.

Table 3. The amount of carbide particles in the microstructure of sample 1 and 2

Sample	Content of carbide particles, %		
	Number of measurements	Mid value, %	Standard deviation
1	5	7.90	1.21
2		12.93	6.51

The amount of carbide particles is higher in sample 2 (12.93 %) compared to sample 1 (7.90 %). In table 4 the carbide particles are classified with respect to the particle size.

Table 4. The classification of particles with respect to the particle size

Particle class	Sample 1			Sample 2		
	Number of particles	Total surface, μm^2	The share of particle class in the total number of particles	Number of particles	Total surface, μm^2	The share of particle class in the total number of particles
1	901	1052.78	0.95	1108	1556.13	0.91
2	41	227.85	0.04	76	451.90	0.06
3	4	40.02	0.004	25	246.04	0.02
4	0	0.00	0.00	10	134.28	0.008
5	0	0.00	0.00	5	87.41	0.005

The total area of detected particles is significantly higher in sample 2 ($2476.76 \mu\text{m}^2$) compared to sample 1 ($1320.65 \mu\text{m}^2$). The area occupied by particles of individual classes is also higher in sample 2 (Table 4). The 946 particles with a total surface area of $1320.65 \mu\text{m}^2$ were detected in sample 1. From the total number of detected particles, most of them were distributed in the first class (901 particles) with an area less than $4.40 \mu\text{m}^2$. In the second class ($4.40 - 8.30 \mu\text{m}^2$) 41 particles were distributed, and in the third class (area $8.30 - 12.20 \mu\text{m}^2$) only 4 particles. The particles from the fourth and fifth particle classes were not detected (Table 4). In sample 2 the 1224 particles with a total area of $2476.76 \mu\text{m}^2$ were detected. Of the total number of detected particles, 1108 were distributed in the first class. The 76 particles were distributed in the second class, 25 particles in the third class, 10 particles in the fourth class and 5 particles in the fifth class (Table 4).

The average particle size was calculated by dividing the total area occupied by particles of each class by the number of detected particles. The sample 1 has the largest amount of first class particles (0.95) with an average particle size of $1.2 \mu\text{m}^2$. The amount of larger class particles (classes between 2 and 5) is significantly lower. The amount of second class particles is 0.04 with an average particle size of $5.6 \mu\text{m}^2$, while the amount of third class particles is 0.004 with an average particle size of $10.0 \mu\text{m}^2$. The highest proportion of first class particles (0.91) with an average particle size of $1.4 \mu\text{m}^2$ was also detected in sample 2. The amount of larger particle class (classes between 2 and 5) is higher compared to sample 1. The amount of second-class particles is 0.06, and the average particle size is $5.9 \mu\text{m}^2$. The average particle size of the third

class is $9.8 \mu\text{m}^2$ and the amount is 0.02. The amount of fourth grade particles with an average size of $13.4 \mu\text{m}^2$ is 0.008, while the amount of fifth grade particles is 0.005 and the average size is $17.5 \mu\text{m}^2$.

The results of the apparent austenitic grain size are given in Table 5.

Table 5. The apparent austenite grain size of the samples 1 and 2 according to ASTM E 112-10

Sample	Length of the reference line (L), mm	Number of intersects (P_i)	Average grain size, μm^2	Apparent austenite grain size (G) number
1	265,9	75	0.224	9
2	345,3	55	0.184	9

The results of the grain size measurements indicate that both samples have fine grade microstructure with the G of 9. The sample 1 has slightly higher grain size ($0.224 \mu\text{m}^2$) compared to sample 2 ($0.184 \mu\text{m}^2$).

The results of microhardness measurements

The results of microhardness measurements of samples 1 and 2 are given in Table 6.

Table 6. The results of microhardness measurements

Sample	Number of measurements	Microhardness, HV			
		The area of the defect		Non-affected area	
		Mid value, HV	Standard deviation	Mid value, HV	Standard deviation
1	3	696.6	9.99	700.1	8.35
2		741.1	1.76	741.2	2.8

In sample 1 higher hardness was measured in the non-affected area (700.1 HV) in relation to the area of the defect (696.6 HV), while in sample 2 almost the same value of hardness was measured in the area of the defect (741.1 HV) and non-affected area (741.2 HV). At both measurement locations, the microhardness of sample 2 is higher compared to the microhardness of sample 1. The higher microhardness of sample 2 is a consequence of higher amount of carbide particles.

CONCLUSIONS

The research was performed on two samples of ASIS M2 high-speed tool steel punches to estimate the cause of the shorter service life of sample 2 compared to sample 1. The cracking occurred after 50.000 punched marks (sample 1) and 20.000 punched marks (sample 2).

The results of chemical composition analysis, metallographic analysis and microhardness measurements led to the following conclusions:

The higher amount of carbide forming elements in sample 2 led to the solidification of higher number of eutectic carbides and precipitation of secondary carbides in intercellular regions. The quantitative microstructure analysis indicated significantly higher number of carbide particles in sample 2 ($2476.76 \mu\text{m}^2$) compared to the sample 1 ($1320.65 \mu\text{m}^2$). The area occupied by carbide particles of individual particle classes is also higher in sample 2. The presence of carbide particles led to the texture development. Since texture orientation is perpendicular to the work surface of the samples, it influenced crack propagation direction. Higher amount of carbide particles in sample 2 caused higher crack dissipation and material layering with a decrease in crack propagation depth.

Acknowledgments

The investigation was performed within the research topic “Design and Characterization of Innovative Engineering Alloys”, Code: FPI-124- 2019-ZZB funded by University of Zagreb within the Framework of Financial Support of Research, scientific-research project within Croatian-Slovenian collaboration “Design and Characterization of Innovative Aluminum - Magnesium - Lithium alloy” (2018-2019) funded by Ministry of Science and Education and Infrastructural scientific projects: Center for Foundry Technology, Code: KK.01.1.1.02.0020 and VIRTULAB - Integrated Laboratory for Primary and Secondary Raw Materials, Code: KK.01.1.1.02.0022 funded by European Regional Development Fund, Operational Programme Competitiveness and Cohesion 2014 - 2020.

Personal gratitude to colleagues from DIV GRUPA d.o.o. for the given samples and enabled publication of the analysis results.

REFERENCES

- [1] M. Cabibbo, N. Clemente, F. Musharavati, S. Spigarelli, Thermal plasticity index of nanostructured N-based coatings on HSS 6-5-2 (1.3343) tool steel, *Material Science Forum*, 879(2017), pp. 262–267, 2017.
- [2] R. Agnelli Mesquita, *Tool Steels: Properties and Performance*, CRC Press, Boca Raton, 2016.
- [3] P. L. C. Serra, R. R. M. Sousa, J. R. Barros Neto, M. S. Libório, M. C. Feitor, T. H. C. Costa, Application of nitriding and duplex treatment on steel drills-HSS, *J Journal of Multidisciplinary Engineering Science*, 7(2020)4, pp. 11699–11708.
- [4] S. Kalyanakumar, C. Munikumar, S. Govind Nair, S. Shaju, Application of multi response optimization of drilling setting main process parameter using VIKOR approach, *Materials Today: Proceedings.*, In press(2020).
- [5] J. Jiang, W. Bao, Z. Y. Peng, X. H. Dai, Creep Property of TMCP High-Strength Steel Q690CFD at Elevated Temperatures, *Journal of Materials in Civil Engineering*, 32(2020)2.
- [6] A. M. Bayer, B. A. Becherer, T. Vasco, *Bulletin: High Speed Tool Steels*, Latrobe Specialty Steel, 16(1989), pp. 10–11.
- [7] ASTM A 600 - 92a (Reapproved 2004), *Standard Specification for Tool Steel High Speed*.
- [8] P. Jovicevic-Klug, B. Podgornik, Comparative study of conventional and deep cryogenic treatment of AISI M3:2 (EN 1.3395) high-speed steel, *Journal of Materials Research and Technology*, 9(2020)6, pp. 13118–13127.
- [9] M. M. Serna, E. R. B. Jesus, E. Galego, L. G. Martinez, H. P. S. Corrêa, J. L. Rossi, An

Overview of the Microstructures Present in High-Speed Steel -Carbides Crystallography, Materials Science Forum, 530–531(2006), pp. 48–52.

- [10] T. Maurizi Enrici, A. Mertens, M. Sinnaeve, J. T. Tchuindjang, Elucidation of the solidification sequence of a complex graphitic HSS alloy under a combined approach of DTA and EBSD analyses, *Journal of Thermal Analysis and Calorimetry.*, 141(2020)3, pp. 1075–1089.
- [11] K. C. Hwang, S. Lee, H. C. Lee, Effects of alloying elements on microstructure and fracture properties of cast high speed steel rolls part I: Microstructural analysis, *Materials Science and Engineering: A*, 254(1998)1–2, pp. 282–295.
- [12] Y. Luan, N. Song, Y. Bai, X. Kang, D. Li, Effect of solidification rate on the morphology and distribution of eutectic carbides in centrifugal casting high-speed steel rolls, *Journal of Materials Processing Technology*, 210(2010)3, pp. 536–541.
- [13] M. Madej, High speed steel based composites with iron additions, *Kovové Materiály*, 50(2012)4, pp. 235–241, 2012.
- [14] T. Kivak U. Şeker, Effect of cryogenic treatment applied to M42 HSS drills on the machinability of Ti-6Al-4V alloy, *Materials and Technology*, 49(2015)6, pp. 949–956.
- [15] Y. Luan, N. Song, X. Kang, D. Li, A study of the carbides in high-speed steel rolls, *Materials Science Forum*, 638–642(2010)January, pp. 3356–3361.
- [16] D. W. Hetzner, W. Van Geertruyden, Crystallography and metallography of carbides in high alloy steels, *Materials Characterization*, 59(2008)7, pp. 825–841.
- [17] Atomic Weight of Molybdenum | Commission on Isotopic Abundances and Atomic Weights." <https://ciaaw.org/molybdenum.htm> (accessed Apr. 07, 2021).
- [18] Atomic Weight of Tungsten | Commission on Isotopic Abundances and Atomic Weights." <https://ciaaw.org/tungsten.htm> (accessed Apr. 07, 2021).
- [19] J. Tchoufang Tchuindjang, M. Sinnaeve, J. Lecomte-Beckers, Influence of High Temperature Heat Treatment on in situ Transformation of Mo-rich Eutectic Carbides in HSS and Semi-HSS Grades, *Proceedings of the international conference Abrasion 2011*, (J. Lecomte-Beckers, J. T. Tchuindjang), ULg-Service MMS, 21.-24.8., 2011, Liege, Belgium.
- [20] A. Çiçek, T. Kivak, E. Ekici, Optimization of drilling parameters using Taguchi technique and response surface methodology (RSM) in drilling of AISI 304 steel with cryogenically treated HSS drills, *Journal of Intelligent Manufacturing*, 26(2015)2, pp. 295–305.
- [21] M. Kuřík, J. Lacza, T. Vlach, J. Sobotová, Study of the properties and structure of selected tool steels for cold work depending on the parameters of heat treatment, *Materials and Technology*, 51(2017)4, pp. 585–589.
- [22] S.A Afolalu, O.P. Abioye, E.Y. Salawu, I.P. Okokpujie, A.A Abioye, O.A. Omotosho, O.O. Ajayi Impact of heat treatment on HSS cutting tool (ASTM A600) and its behaviour during machining of mild steel (ASTM A36), *AIP Conference Proceedings*, (P. L. Verma, V. B. Tungikar and Y. J. Bhalerao), 5–6 July, 2018, Maharashtra, India.